

1 SUB-MILLIMETRE RESOLUTION LAMINAR FMRI USING

2 ARTERIAL SPIN LABELLING IN HUMANS AT 7 T

3 *Author list:*

4 Sriranga Kashyap ^{a, b *}

5 Dimo Ivanov ^{a, b *}

6 Martin Havlicek ^a

7 Laurentius Huber ^{a, b}

8 Benedikt A. Poser ^{a, b}

9 Kâmil Uludağ ^{c, d, e}

10

11 *Affiliations:*

12 ^a Department of Cognitive Neuroscience, Faculty of Psychology and Neuroscience, Maastricht
13 University, Maastricht, The Netherlands

14 ^b Maastricht Brain Imaging Centre (M-BIC), Maastricht University, Maastricht, The Netherlands

15 ^c Center for Neuroscience Imaging Research, Institute for Basic Science, Sungkyunkwan University,
16 Suwon, South Korea

17 ^d Department of Biomedical Engineering, N Center, Sungkyunkwan University, Suwon, South Korea

18 ^e Techna Institute & Koerner Scientist in MR Imaging, University Health Network, Toronto, Canada

19 * These authors contributed equally to this work

20

21 *Correspondence to:*

22 Department of Cognitive Neuroscience,

23 Faculty of Psychology & Neuroscience,

24 Maastricht University

25 PO Box 616

26 6200MD Maastricht

27 The Netherlands

28 sriranga.kashyap@maastrichtuniversity.nl, kamil.uludag@rmpuhn.ca

29

30 ABSTRACT

31 Laminar fMRI at ultra-high magnetic field strength is typically carried out using the
32 Blood Oxygenation Level-Dependent (BOLD) contrast. Despite its unrivalled
33 sensitivity to detecting activation, the BOLD contrast is limited in its spatial specificity
34 due to signals stemming from intra-cortical ascending and pial veins. Alternatively,
35 regional changes in perfusion (i.e., cerebral blood flow through tissue) are
36 colocalised to neuronal activation, which can be non-invasively measured using
37 arterial spin labelling (ASL) MRI. In addition, ASL provides a quantitative marker of
38 neuronal activation in terms of perfusion signal, which is simultaneously acquired
39 along with the BOLD signal. However, ASL for laminar imaging is challenging due to
40 the lower SNR of the perfusion signal and higher RF power deposition i.e., specific
41 absorption rate (SAR) of ASL sequences. In the present study, we present for the
42 first time in humans, isotropic sub-millimetre spatial resolution functional perfusion
43 images using Flow-sensitive Alternating Inversion Recovery (FAIR) ASL with a 3D-
44 EPI readout at 7T. We show that robust statistical activation maps can be obtained
45 with perfusion-weighting in a single session. We observed the characteristic BOLD
46 amplitude increase towards the superficial laminae, and, in apparent discrepancy,
47 the relative perfusion profile shows a decrease of the amplitude and the absolute
48 perfusion profile a much smaller increase towards the cortical surface. Considering
49 the draining vein effect on the BOLD signal using model-based spatial ‘convolution’,
50 we show that the empirically measured perfusion and BOLD profiles are, in fact,
51 consistent with each other. This study demonstrates that laminar perfusion fMRI in
52 humans is feasible at 7T and that caution must be exercised when interpreting BOLD
53 signal laminar profiles as direct representation of the cortical distribution of neuronal
54 activity.

55 **Keywords:**

56 ultra-high field MRI, laminar fMRI, arterial spin labelling, perfusion, fMRI signal model

57

58 INTRODUCTION

59 Neuronal activity in the brain is associated with an increased metabolic demand
60 accompanied by changes in haemodynamics such as blood oxygenation, flow and
61 volume (for reviews see: [1–4]). Functional magnetic resonance imaging (fMRI) is a
62 technique that can non-invasively measure these changes and allows inferring the
63 spatial pattern of neuronal activity while performing a task or at rest. Improvements
64 in MRI technology over the past decades, such as higher magnetic field strengths,
65 novel sequences, optimised pulse designs, and parallel imaging, have pushed the
66 spatial and temporal limits to an extent wherein MRI at ultra-high magnetic field
67 (UHF, $\geq 7\text{T}$) can routinely achieve sub-millimetre spatial resolution voxels in humans,
68 for both structural and functional imaging (see Special Issues: [5,6] and reviews
69 therein). While fMRI investigations have yielded robust, reproducible functional
70 parcellation [7] of different brain areas consistent with previous *ex vivo* cyto- and
71 myelo-architectural studies [8,9], the advantages of UHF fMRI have enabled
72 neuroscientists to investigate the mesoscopic circuitry within regions across cortical
73 depths and, to a lesser extent, columns in humans (see Special Issue: [10] and
74 reviews therein).

75 A vast majority of standard-resolution and laminar fMRI studies have been
76 performed using the Blood Oxygenation Level-Dependent (BOLD) contrast [11,12].
77 While the BOLD contrast excels in its sensitivity to detect signal changes due to its
78 high signal-to-noise (SNR), it is inherently limited in its spatial specificity relative to
79 site of neuronal activation because of strong signal bias introduced via the intra-
80 cortical ascending veins [13] and by the non-local signal spread (drainage effect)
81 through pial veins [14,15]. Studies investigating the specificity of the laminar BOLD

82 response in humans and animals [16–20] have consistently observed the largest
83 signal change in the BOLD signal at the superficial layers and pial surface despite
84 the fact that the peak of the neuronal activity is expected in the input layers (layer IV
85 in human V1) for feed-forward stimuli [21,22]. Some earlier studies have investigated
86 the leakage of the signal between laminae during steady-state [22–24]. Recently, a
87 fully dynamical model of the laminar BOLD signal has been developed [13] that
88 enables model-driven “deconvolution” (i.e. removal of the intra-cortical ascending
89 venous signal) of the measured BOLD signal profiles to unravel the underlying
90 neuronally-driven signal profiles. However, theoretical assumptions of these model-
91 driven approaches have not yet been subjected to experimental validation.

92 The versatility of MRI provides the means to also measure other (non-BOLD)
93 haemodynamic response parameters such as cerebral blood volume (CBV) using
94 vascular space occupancy (VASO) [25–27] or cerebral blood flow (CBF) through
95 tissue (perfusion) using arterial spin labelling (ASL) [28–30]. Most studies using
96 these non-BOLD approaches have been carried out in animal models [3,4,31] and
97 have only been applied to high-resolution human studies with the advent of UHF
98 fMRI [32–34]. From the perspective of laminar fMRI, animal studies have shown that
99 perfusion-weighting is a highly desirable contrast, even more so than total CBV, due
100 to its spatial proximity to neuronal activation [18,35]. While CBV-weighted imaging
101 using VASO has seen a resurgence for laminar fMRI applications [36], perfusion-
102 weighted fMRI using ASL has been mostly limited to relatively low spatial resolution
103 (\cong 2–4 mm) studies [37] (but see [38]). Achieving higher spatial resolutions, let alone
104 sub-millimetre resolutions, with perfusion-weighting and adequate brain coverage is
105 challenging. This is due to the relatively lower SNR of the perfusion-weighted signal
106 owing to the low microvascular density and T_1 recovery of the labelled arterial water

107 signal, and the higher RF power deposition of ASL sequences in general. The SNR
108 limitation can be addressed to some extent by moving to UHF. The gain in SNR due
109 to increased field strength [39] and the prolonged longitudinal relaxation times (T_1)
110 [40,41] allows longer post-labelling delays, thereby, improving the perfusion SNR
111 [33]. Recent developments using ASL at 7 T [32,33,42–44] have enabled pushing
112 the spatial resolution for perfusion-mapping to the sub-millimetre regime [45,46] by
113 overcoming several technical challenges; i.e. optimisation of sequence and pulse
114 design [34,44,47], using dielectric pads [48] in order to improve the labelling
115 efficiency [33], and utilisation of a 3D-EPI readout [49].

116 Taking together these advantages at UHF, the spatial specificity of the perfusion
117 signal and the fact that ASL acquires both BOLD and perfusion-weighted images
118 simultaneously makes ASL a very attractive tool for laminar fMRI. In the present
119 study, we build on our previous work to acquire, for the first time, sub-millimetre
120 resolution simultaneous BOLD and perfusion-weighted fMRI of the human visual
121 cortex at 7T. We demonstrate that robust, participant-specific, single-session, high-
122 resolution perfusion activation maps can be obtained for laminar fMRI in humans at
123 7T. We probe the cortical depth-dependence of BOLD and perfusion-weighted
124 signals in response to visual stimulation in humans and reconcile our experimental
125 findings using the recently proposed dynamic model of the laminar BOLD signal.

126

127 **METHODS**

128 Seven healthy volunteers (median age=28 years) participated in the study following
129 screening and having given written informed consent. The study was approved by
130 the Ethics Review Committee for Psychology and Neuroscience (ERCPN) at
131 Maastricht University and all procedures followed the principles expressed in the
132 Declaration of Helsinki.

133 **Data acquisition**

134 Data were acquired on a whole-body Siemens Magnetom 7T research scanner with
135 a gradient system capable of maximum gradient amplitude of 70 mT/m and
136 maximum slew rate of 200 T/m/s (Siemens Healthineers, Erlangen, Germany) and a
137 32-channel receive phased array head coil (Nova Medical, USA). The participant
138 placement and preparatory procedure followed the protocol previously described in
139 [33,42]. In short, the eye centres were taken as iso-centre reference (instead of the
140 eyebrows, as is typically done) and supplementary cushions were provided to the
141 participants under the neck, to ensure that the large feeding arteries to the brain
142 were parallel to the B_0 . In addition, two 18x18x0.5 cm³ high-permittivity dielectric
143 pads containing a 2.8:1 solution of calcium titanate (CaTiO₃) and heavy water (D₂O)
144 by weight [50] were placed on either side of the head at the level of the participant's
145 temporal lobes to increase B_1 (therefore, labelling) efficiency at 7T [51].

146 **Stimulus paradigm:** Full contrast black-and-white radial flickering checkerboard
147 was presented using PsychoPy v 1.90.0 [52] for 20 s (stimulus on) followed by 40 s
148 of an iso-luminant grey background (stimulus off). Each functional run lasted ~12
149 minutes consisting of a 30 s initial baseline period and ten stimulus on-off blocks.

150 The participants were instructed to remain motionless and fixate on a central fixation
151 dot throughout each of the four functional runs.

152 **Anatomical MRI:** Anatomical data were acquired using a 3D-MP2RAGE [53] at 0.9
153 mm isotropic spatial resolution (192 sagittal slices; GRAPPA = 3; FoV_{read} = 230 mm;
154 phase-encoding = A>>P; TI₁/TI₂ = 900/2750 ms; a₁/a₂ = 5°/3°; TE/TR = 2.39/4500
155 ms; partial-Fourier_{phase} = 6/8; bandwidth = 250 Hz/px; echo-spacing = 6.6 ms, TA = 6
156 min).

157 **Functional MRI:** Functional data were acquired at 0.9 mm isotropic resolution using
158 a pulsed ASL (PASL) sequence [29] with a 3D-EPI readout [49] employing a FAIR
159 [54] QUIPSS II [30] labelling scheme (44 axial slices; GRAPPA = 4; FoV_{read} = 192
160 mm; phase-encoding = A>>P; TE/TR = 15/2850 ms; a=19°; TI1/TI2 = 700/1891 ms;
161 partial-Fourier_{phase} = 5/8; partial-Fourier_{slice} = 7/8; Ref. lines PE = 64; Ref. scan mode
162 = FLASH [55]; bandwidth = 1124 Hz/px; echo-spacing = 1.02 ms, repetitions = 230,
163 TA =11 min). The labelling was achieved using a tr-FOCI inversion pulse [47] (10ms)
164 that provided efficient (up to 95%) slab-selective inversion despite inhomogeneous
165 B₁ and SAR constraints at high field [33,36]. Immediately after each of the four
166 functional runs, five volumes with opposite phase-encoding were acquired for run-
167 wise distortion-correction. All the ASL data were reconstructed using GRAPPA
168 kernel of size {3,2} [42] and 8 iterations of the POCS algorithm [36,56]. The
169 functional data acquisition slab was oriented to cover as much of the occipital lobe
170 as possible in all participants centred on the calcarine sulcus (S3 Fig a).

171 **Data processing**

172 The anatomical data were pre-processed in SPM12 r7487
173 (<https://www.fil.ion.ucl.ac.uk/spm/software/spm12/>) [57,58] and FSL v. 6.0

174 (<https://fsl.fmrib.ox.ac.uk/fsl/fslwiki>)[59,60]. This anatomical pre-processing workflow was
175 developed particular to work well for MP2RAGE data. First, the second inversion
176 image of the MP2RAGE was subjected to the automated segmentation in SPM12
177 [61]. The bias-corrected second inversion image was used to create a whole-brain
178 mask using FSL BET [62]. The thresholded non-brain tissue classes from the
179 SPM12 segmentation were summed together to create a mask of the non-brain
180 tissue and large sinuses (for illustration of the analysis steps, see S1 Fig). The non-
181 brain mask was manually curated in cases, in which the automatic masks were sub-
182 optimal. The T1-w MP2RAGE image was bias-corrected using SPM12 and was
183 stripped off the non-brain tissue and large sinuses using the mask obtained from the
184 second inversion image. This pre-processed T1-w MP2RAGE was supplied as input
185 to the high-resolution *recon-all* pipeline of Freesurfer v.6.0
186 (<https://surfer.nmr.mgh.harvard.edu/>) [63]. Additionally, the MP2RAGE T1 map was
187 supplied as an additional input (T2-w proxy) to Freesurfer for pial surface
188 optimisation. The segmentation and surface construction were done in the native
189 resolution and the segmentation quality in the occipital lobe was manually curated. A
190 probabilistic retinotopic atlas was applied to the Freesurfer reconstructed data using
191 *neuropythy* (<https://github.com/noahbenson/neuropythy>) [64] to obtain participant-
192 specific V1 and V2 regions-of-interest (ROIs) (S3 Fig b). Following the automatic
193 segmentation and reconstruction, the WM surface was extended into WM by 30% of
194 the cortical thickness to account for any discrepancy of the GM-WM boundary when
195 using T1-w MP2RAGE images[65]. The first inversion image of the MP2RAGE was
196 used to check the extended WM boundaries due to its sharp WM-GM contrast. We
197 also extended the pial boundary by the same amount into the CSF to sample the
198 signal away from the pial boundary. Then, we generated a total of twenty-one

199 intermediate equi-volume surfaces within the GM using Surface tools
200 (https://github.com/kwagstyl/surface_tools) [66] (S3 Fig c).

201 The functional datasets were pre-processed using Advanced Normalization Tools
202 (ANTs) v.2.3.1 (<https://github.com/ANTsX/ANTs>) [67,68]. First, the functional runs
203 were subjected to affine realignment. Next, the temporal mean of the functional run
204 and the temporal mean of the opposite phase-encoded run were used to calculate
205 an undistorted template image and the distortion-correction warps were saved.
206 Lastly, a transformation matrix was calculated for each functional run to the T1-w
207 data using the visual alignment tools in ITK-SNAP v.3.6 [69] and a final rigid
208 alignment using ANTs. All transforms were concatenated and applied to the
209 unprocessed functional datasets in a single resampling step using a 4th degree B-
210 spline interpolation. This workflow was particularly developed keeping in mind the
211 need in laminar fMRI analyses [70]. It minimises resolution losses due to multiple
212 interpolation steps while providing the high-quality registration accuracy that is
213 required in laminar fMRI studies.

214 Statistical analyses of the functional data were carried out using FSL FEAT [71,72]
215 by modelling three regressors i.e., the stimulus design convolved with the canonical
216 haemodynamic response function (HRF) representing the BOLD signal, the
217 alternating label-control acquisition of the ASL sequence representing the baseline
218 perfusion-weighting and the combination of these two regressors representing the
219 perfusion activation. Due to the disparity in the spatial spreads of the BOLD and
220 perfusion activation (Fig 2), a mask of the overlap between the BOLD and perfusion
221 activation cluster thresholded masks from FEAT was created. This ensured that we
222 sampled the BOLD and perfusion signals from the same voxels.

223 Laminar analyses were carried out in Freesurfer by sampling the functional time-
224 series signal from the ROIs using nearest-neighbour interpolation. No surface or
225 intra-cortical smoothing was applied. The laminar time-courses sampled from V1 and
226 V2 across all participants were imported into MATLAB R2016b (MathWorks, USA)
227 for the time-series analyses. The BOLD and perfusion-weighted time-courses were
228 obtained for each lamina by applying surround-averaging and surround-subtraction,
229 respectively [73–75] and the event-related average time-courses were calculated.
230 The event-related average BOLD time-course was subsequently rescaled to percent
231 BOLD signal change relative to the pre-stimulus baseline (~10 s). The analysis of the
232 perfusion time-series followed several steps: First, the perfusion-weighted time-
233 series is a measure of the modulation depth (or the magnitude of the zig-zag) of the
234 raw ASL time-course in MRI signal units (S5 Fig). It is important to note that these
235 data are not scaled in physiological units and is representative of the perfusion SNR
236 of the data. We then derived the following measures from perfusion-weighted time-
237 course: absolute and relative perfusion change, and baseline perfusion. Absolute
238 perfusion change was calculated by taking the change in the perfusion activation
239 (i.e., by subtracting the pre-stimulus baseline) per lamina and then normalising the
240 signal with the mean of the EPI (to account for transmit-receive biases). The
241 absolute perfusion change, thus obtained, is in arbitrary units but proportional to the
242 quantitative perfusion change. The absolute perfusion change can then be rescaled
243 into physiological units, as typically done in perfusion quantification studies [37,76].
244 Relative perfusion change is the percentage change in the perfusion signal due to
245 activation per depth relative to its respective baseline. Note that the relative
246 perfusion change does not need to be divided by the mean EPI image for scaling (as
247 it appears both in the nominator and the denominator and thus cancels out). The

248 baseline perfusion (Fig 1) was calculated using simple subtraction of the label-
249 control time-points during the baseline period (~0-30 s at the beginning of the run)
250 and pre-stimulus intervals (~0-10 s before stimulus onset) of the stimulus blocks.
251 Laminar steady-state profiles of the BOLD signal, absolute, and relative perfusion
252 change signals were calculated by averaging the respective signals within the ~14-
253 28 s interval following stimulus onset. The baseline perfusion laminar profile (S4 Fig)
254 was obtained by averaging within the entire the ROIs.

255 **Simulating the laminar BOLD signal from the measured perfusion profile**

256 The experimentally measured laminar BOLD response profiles in V1 and V2 regions
257 were compared to theoretical predictions of the dynamical laminar BOLD signal
258 model proposed by Havlicek and Uludağ using publicly available MATLAB code
259 (https://github.com/martinhavlicek/laminar_BOLD_model) and plausible assumptions
260 regarding physiology and acquisition parameters at 7T. The measured absolute
261 perfusion laminar profiles (both baseline and activation) were used to input the
262 physiological parameters of the model. The total amount of venous baseline CBV
263 (CBV_0) was set to 2 mL, of which 50% relates to microvasculature and 50% to the
264 ascending veins. The baseline CBV (CBV_0) distribution was set to be constant
265 across laminae in the microvasculature but increased linearly towards the surface in
266 the ascending veins (slope, $s = 0.4$). The measured baseline perfusion signal in this
267 analysis (CBF_0) is proportional to CBF in physiological units. Assuming that the CBV_0
268 in microvasculature (1 mL /100 g) is divided uniformly between all laminae and the
269 mean transit time through microvasculature (averaged across all laminae) is ~1 s
270 (also see Table 2), a scaling factor $x = 5520$ was estimated such that an average
271 $CBF_0 \sim 60$ mL /min/100 g was obtained. Given the variation of CBF_0 across laminae,

272 the lamina-specific transit times through microvasculature varied between ~0.6 s
273 near the superficial laminae to ~1.2 s in the deeper laminae (0.5 s variation in transit
274 time through capillaries between superficial and deeper laminae). The lamina-
275 specific transit times through ascending veins were then calculated using the central
276 volume principle (for details, see [13]). Lamina-specific changes in relative CMRO₂
277 were obtained by assuming a linear coupling ($n = 3$) between CBF and CMRO₂ [77].
278 All other parameters were defined as in the default scenario described in [13].
279 Please note that we did not fit the model to data but used experimentally obtained
280 perfusion-weighted signal data and plausible biophysical parameters to generate a
281 prediction of the laminar BOLD signal profile.

282

283 RESULTS

284 **Baseline perfusion:** Fig 1a and b show two representative slices (one superior, one
285 inferior) of the average baseline perfusion map and the perfusion temporal signal-to-
286 noise (tSNR) of a participant overlaid on the T₁-w anatomical image. These maps
287 show that the average perfusion signal is highly localised to the GM ribbon and
288 demonstrates the quality of the co-registration between the acquisition slab with the
289 anatomy as indicated by the absence of signal shifted into the ventricles and the
290 clearly defined sulci (wherever resolvable). The perfusion-weighted data shown in
291 Fig 1a is in arbitrary MRI signal units.

292 **Functional activation:** Robust statistical activation was obtained for all participants
293 for both the BOLD (Fig 2a) and perfusion signals (Fig 2b). The BOLD activation
294 envelopes a much larger swath of cortex than perfusion activation does (Fig 2a, 2b,
295 left panel). This is expected given the differences in the detection sensitivity (i.e.
296 functional contrast-to-noise (fCNR)) between the BOLD and perfusion signals and
297 the presence of BOLD signal in pial veins.

298 In addition, the BOLD activation obtained follows the characteristic localisation
299 pattern observed with standard GE-EPI studies. That is, the largest BOLD activated
300 voxels are always localised at the CSF-GM boundary (Fig 2a, purple zoomed-out
301 boxes). In contrast, the perfusion activation was observed to be more spatially
302 localised to the GM ribbon with the highest activated voxels localised mid- to deep-
303 GM (Fig 2b, green zoomed-out boxes). The activation maps are shown in the three
304 orthogonal views to highlight the consistency of the GM localisation of activation in
305 3D.

306 Finally, the ASL time-courses exhibit a zig-zag modulation that is characteristic of
307 ASL sequences (due to the acquisition of alternating label and control volumes)
308 demonstrating the high quality of the data. The modulation depth of this zig-zag
309 represents the amount of labelled spins delivered to the tissue and is, therefore,
310 proportional to tissue perfusion. In Fig 2 (purple), the ASL time-course obtained from
311 the highest BOLD signal activated voxels shows the typically observed increase in
312 the BOLD signal magnitude during activation with weaker zig-zag modulation. On the
313 other hand, the ASL time-course obtained from the highest perfusion-activated
314 voxels (Fig 2, green) shows the strong zig-zag modulation throughout but with lower
315 BOLD signal modulation. All three key differences between the BOLD and perfusion
316 activation signals were consistently observed in all the participants.

317 **Laminar analysis**

318 The group-average laminar time-courses of BOLD signal change, absolute perfusion
319 change, and relative perfusion change are shown in Fig 3 for V1 and in Fig 4 for V2.
320 The temporal behaviour of the three sampled signals across all laminae is presented
321 as a heatmap in the top row with time along the X-axis and the cortical depth along
322 the Y-axis and the magnitude of the signal in colour code. We observed inter-
323 regional differences with laminar responses of all three signals, with V2 having a
324 lower amplitude than V1. The laminar profiles of the BOLD signal change exhibit
325 positive slopes (Slope V1: 4.88 ± 0.129 , Slope V2: 4.81 ± 0.195) with a strong linear
326 trend (R^2 V1: 0.986, R^2 V2: 0.967). The laminar profiles of the relative perfusion
327 change, on the other hand, exhibit negative slopes (Slope V1: -4.91 ± 0.27 , Slope
328 V2: -4.64 ± 0.111) with a strong linear trend (R^2 V1: 0.939, R^2 V2: 0.988).
329 Interestingly, the absolute perfusion changes exhibit a moderately positive slope

330 (Slope V1: 3.35 ± 0.68 , Slope V2: 3.80 ± 0.485) albeit without a strong linear trend
331 (R^2 V1: 0.537, R^2 V2: 0.745). In the perfusion signals, slight oscillatory behaviour is
332 observed during the post-stimulus period.

333 **Simulations of the laminar BOLD signal**

334 Fig 5 shows the simulated laminar BOLD signal profile (solid blue lines) and the
335 experimentally measured laminar BOLD signal profiles (dotted purple lines, see Fig
336 3, 4). The measured and simulated profiles were highly congruent (Pearson's
337 correlation: $r = 0.9984$ for V1, $r = 0.9977$ for V2), demonstrating that, despite the
338 discrepancy of the relative & absolute perfusion and the BOLD signal profiles, they
339 are in fact compatible with each other.

340

341 **DISCUSSION**

342 Here, we demonstrated, for the first time in humans, isotropic sub-millimetre spatial
343 resolution perfusion fMRI using ASL. We found incongruent cortical depth profiles
344 between the BOLD signal and perfusion changes, which, however, turned out to be
345 physiologically consistent with each other after employing a dynamical BOLD signal
346 model.

347 **Functional BOLD and perfusion activation**

348 We obtained robust participant-specific, single-session activation maps for
349 simultaneously acquired isotropic sub-millimetre spatial resolution BOLD and
350 perfusion signals at 7T. We observed a larger spread of activation for the BOLD
351 signal (Fig 2a) compared to the perfusion signal (Fig 2b). This is expected because
352 the detection sensitivity of the perfusion signal (fCNR) is much lower than that of the
353 BOLD signal [33,37,38]. Additionally, this can also be explained by the higher spatial
354 specificity of the perfusion signal compared to the BOLD signal, which is susceptible
355 to non-local signal spread due to downstream venous bias away from the actual site
356 of activation [14]. This is also observed in high-resolution fMRI with the highest
357 BOLD activated voxels located at the CSF-GM boundary (Fig 2a). On the other
358 hand, the perfusion activation map exhibits a well-defined localisation to the cortical
359 ribbon (Fig 2b), mostly located in cortical GM [18]. Importantly, given that perfusion
360 signal has much lower fCNR than the BOLD signal in standard resolution studies (2-
361 4 mm in each direction), it was not necessarily expected that ASL will have enough
362 sensitivity at submillimetre resolution for detecting perfusion activation. One reason
363 that with increasing resolution there is enough perfusion fCNR is that not only image
364 SNR but also partial voluming with CSF and WM is decreased, i.e. thermal and

365 physiological noise coming from outside GM are reduced. This is different for the
366 BOLD signal as pial vessels located in CSF (see Fig 2a) do contribute to the overall
367 BOLD signal in low resolution studies and therefore increases in spatial resolution
368 decrease both image SNR and overall signal contribution. That is, going from low- to
369 high-spatial resolution penalizes CNR of the BOLD signal more than of the perfusion
370 signal.

371 Recently, a novel fMRI approach called VAPER [78] has also been put forward as a
372 contrast useful for perfusion-weighted high-resolution fMRI by mixing VASO and
373 perfusion contrasts. Although the combination of two contrasts boosts VAPER's
374 sensitivity, it markedly complicates its ability to quantify perfusion but also, its
375 physiological specificity. Thus, established ASL techniques remain the most feasible
376 way to acquire *in vivo* perfusion-weighted images that can be straightforwardly
377 validated using quantitative fMRI models, and can be expected to provide
378 reproducible results across a wide range of sequence parameters and field strengths
379 [33]. In this regard, the present study is the first demonstration in humans of the
380 improved spatial specificity of the perfusion signal compared to the BOLD signal
381 using ASL at a sub-millimetre spatial resolution.

382 A recent review of non-BOLD laminar fMRI methods illustrated the potential of the
383 3D-EPI PASL sequence for perfusion-weighted laminar fMRI applications at ultra-
384 high field. As highlighted in the review, the perfusion contrast has been highly
385 desired for laminar fMRI [79] as the perfusion signal is relatively unaffected by the
386 venous compartments, both by the pial and ascending veins, and the large arterial
387 compartments. In comparison, the BOLD signal is heavily weighted towards the
388 venous compartments and the VASO signal can have contributions from both arterial

389 and venous in addition to microvasculature CBV changes [34,80,81]. The reason for
390 the high perfusion localisation specificity is that the tagged arterial water is mostly
391 exchanged with the tissue at the level of the capillaries. In addition, the transit delay
392 for the labelled blood to arrive at the region-of-interest (in this case, occipital lobe)
393 can be ~1-1.3 s [82]. Together with the blood transit time within tissue on the order of
394 ~1-2.5 s [83] only little longitudinal magnetisation of the tag remains (due to T1
395 decay), i.e. that almost no magnetisation of the label is present in venous blood (see
396 S8 Fig), except for artefacts caused by labelling of venous blood superior to the
397 imaging slab in some ASL schemes (see [76]). The transit time for the acquisition in
398 the present study was optimised for the visual cortex and is reflected in the inter-
399 regional differences in the baseline perfusion signal and its temporal stability of the
400 tissue (Fig 1). The absence of the venous bias and the signal being dominated by
401 the capillary compartment implies that the perfusion contrast more closely follows
402 both the spatial profile and the amplitude of cortical metabolism and neuronal
403 activation. Another important aspect of ASL acquisitions is the possibility to obtain a
404 quantitative estimate of the baseline signal across depths.

405 The difference between the highly BOLD-activated or highly perfusion-activated
406 voxels is readily visible in the ASL time-courses (see Fig 2). The time-courses for
407 perfusion activation show reduced amplitude of the signal envelope and larger
408 difference between pairs of data points (i.e. the zig-zag modulation) indicating that
409 these voxels contain signals from mostly the microvasculature and that observed
410 responses are indeed capturing the changes in perfusion. In contrast, there are small
411 zig-zag changes relative to the overall signal envelope in the time-courses for the
412 highest BOLD activation, reflecting a smaller contribution from microvasculature.
413 This means that the spatial non-overlap that we observe between the perfusion and

414 BOLD signals is driven largely by differences in the underlying physiology and not
415 the differences in SNR.

416 **Laminar BOLD and perfusion responses**

417 We replicated previous findings [21,84,85] that the event-related average BOLD
418 signal amplitude (Fig 3 and 4, first column) increases towards the CSF-GM boundary
419 (e.g., [86,87]). The BOLD signal increase to the superficial layers is well understood
420 and can be attributed to two signal biases: a) increase in baseline CBV of the intra-
421 cortical ascending veins and b) the non-local blooming effect from the pial veins
422 ([88], and for overview see, [2]). The presence of these biases in the BOLD signal
423 makes the interpretation of the measured laminar signal profile, specifically in the
424 superficial layers, challenging [89]. One approach to deal with the issue of spatial
425 bias in GE-BOLD signal is model-driven spatial “deconvolution” [22,24] , which,
426 however, has not yet been validated with another (simultaneously) acquired fMRI
427 modality.

428 The profile of the relative perfusion change (Fig 3 and 4, right column) exhibits the
429 opposite behaviour (compared to the BOLD profile) with the magnitude of the signal
430 increasing towards the GM-WM boundary with a strong linear trend. Furthermore,
431 QUIPSS II pulses were employed in the present study allowing clear-cut definition of
432 the tagged bolus. This means that the observed patterns of laminar signal behaviour
433 are unlikely to be due to undelivered tagged blood in the diving arterioles. Although
434 the impact of the QUIPSS II pulse depends on the chosen parameters and the arrival
435 times to the regions-of-interest, an increase in blood flow upon activation can result
436 in a more complete delivery of the tagged spins to the tissue, including the deeper
437 layers at the time of volume acquisition. This could yield a larger fractional perfusion

438 change in the deeper layers relative to the baseline condition. While it is usually
439 argued that for feed-forward stimuli the peak in activation must be in the middle
440 layers, electrophysiological evidence, histology, and a previous BOLD signal study
441 after spatial “deconvolution” (Marquardt et al., 2018) support the view that V1 also
442 receives high input into layer VI in addition to layer IV. Please note that despite the
443 high spatial resolution used in this study, we do not detect a fine-grained distinction
444 between laminae. The perfusion spatial profile obtained, thus, represents a
445 smoothed version of the underlying neuronal activity. For example, data shown in Fig
446 4b and 4d in [22] and in [90] (see Fig 9 in [22]) are compatible with the spatial
447 profiles found in the current study. We find that the relative increase in the perfusion
448 signal in the middle to deeper layers is also consistent with animal literature (see
449 also [18,91,92]).

450 The absolute perfusion signal change profile (Fig 3 and 4, middle column) exhibits a
451 weak positive slope and non-linear behaviour across depths. However, both relative
452 and absolute signal changes are derived from the same perfusion-weighted signal
453 obtained after surround-subtraction and the difference stems from the spatial profile
454 of the baseline perfusion (S5 Fig). Please note, that the increase of the absolute
455 perfusion signal from WMB to CSFB (by ~30-50%) is much smaller than that of the
456 BOLD signal (by ~100-120%). Additionally, in contrast to the BOLD signal, the
457 absolute perfusion change drops beyond the CSF border. Taken together, the
458 relative and absolute perfusion signal changes differ in their depth-dependent
459 behaviour and both differ from the BOLD signal either in the sign of their slope or the
460 relative increase of the profile towards the surface.

461 In order to test if this discrepancy between the relative & absolute perfusion profiles
462 and BOLD profile can be reconciled, we simulated the BOLD signal profile from the
463 measured perfusion profiles using the recent dynamical laminar BOLD signal model
464 (for details, see S4 Fig). We show that the positive slope and the relative increase of
465 the measured BOLD profile can be obtained from the laminar profile of the relative
466 (having negative slope) and absolute (having much smaller increase towards the
467 surface) perfusion signal by modelling the ascending vein bias, i.e., simulating the
468 laminar BOLD response in a forward manner. Therefore, we conclude that despite
469 their seemingly contrasting behaviours, the BOLD and perfusion signal profiles are,
470 in fact, physiologically consistent with each other.

471 Additionally, the BOLD time-courses exhibit a strong post-stimulus undershoot (PSU)
472 consistent with previous studies [84,93]. Interestingly, our perfusion measures also
473 exhibit PSUs but with smaller amplitudes relative to the positive response. In
474 contrast to the smooth recovery of the PSU to baseline in the BOLD signal, the
475 perfusion PSU exhibits slight oscillatory behaviour. These post-stimulus oscillatory
476 transients are consistent with previous reports of perfusion measurements in
477 humans (e.g., [94]) and with optical imaging in rodents [95]. The oscillatory transients
478 observed in the previous perfusion study in humans [94] could not resolve any
479 depth-dependent modulations owing to its much lower spatial resolution (i.e. 2.65 x
480 2.65 x 5 mm³). The post-stimulus oscillations in our study near the WM boundary are
481 smoother and evolve with a different oscillatory phase than near the CSF boundary,
482 where the oscillations are more pronounced (Fig 3 and 4, middle panels). While it is
483 interesting, pin-pointing the exact vascular physiology that elicits this behaviour is
484 beyond the scope of this study.

485 Taken together, we believe that the current study presents a breakthrough in non-
486 BOLD fMRI research with the development of sub-millimetre resolution perfusion
487 fMRI using ASL and its feasibility for layer-specific investigations, which has hitherto
488 been an uncharted territory in humans.

489 **Data processing**

490 We developed a novel workflow to pre-process anatomical images (S1 Fig) by using
491 the second inversion image of the MP2RAGE and SPM's segmentation to
492 automatically mask out the sagittal and transverse sinuses that are crucial for highly
493 accurate pial surface delineation using Freesurfer's recon-all. In some participants,
494 the workflow required (albeit very little) manual corrections of the segmentation
495 masks. Additionally, we supplied the quantitative T1 map of the MP2RAGE as a
496 proxy T2 in the recon-all stage 3 to further improve the pial surface reconstruction.
497 We used an open-source python package *neuropythy* [64] to apply a probabilistic
498 atlas of retinotopy in participant's native space to generate automatic labels of V1
499 and V2 (S3 Fig b). We qualitatively compared this atlas-based approach on a
500 separate dataset of pRF mapping that was acquired using the same scanner, head
501 coil and similar coverage (data not shown) and found high degree of overlap. Please
502 note, the focus of the present work is distinguishing the BOLD and perfusion signals
503 and does not rely on the perfect delineation of V1 and V2 borders. Cortical layering
504 was done using the equi-volume approach [96] using *Surface tools* [97] as equi-
505 volumetric layering is not natively supported in Freesurfer. Nevertheless, for spatial
506 resolutions such as the present study the exact choice of the layering model does
507 not affect our main conclusions [98]. Even though the layering is done on the whole
508 cortical ribbon, we manually ensured that the delineations were accurate within the

509 V1 and V2 masks in each participant. As ASL measures the BOLD signal
510 simultaneously with perfusion, the BOLD signal profile serves as an internal control
511 for the accuracy of the segmentation and layering. The BOLD signal spatial profile
512 for feed-forward stimuli (such as checkerboards as used in this study) is well known
513 and the BOLD signal derived from the ASL data reproduces this well-known
514 amplitude increase towards the surface of the cortex (see Fig 3 and 4), confirming
515 the accuracy of the data processing in this study.

516 We have previously encouraged studies to align anatomical-to-functional data in
517 order to reduce the blurring due to the application of several resampling steps on the
518 high-resolution, high-fidelity laminar fMRI datasets [84]. While minimal processing
519 approaches for fMRI have been proposed [99], as far as we know, they have not
520 been applied to laminar fMRI. To this end, our workflow using the ANTs framework
521 estimates, combines and applies transformations of motion, distortion-correction and
522 co-registration to the anatomical image in a single resampling step, thereby reducing
523 the amount of smoothing resulting from the processing of the data. Please note, in
524 some ASL acquisitions there may be strong differences in image contrast between
525 the label and control images and the choice of realignment cost-function may impact
526 the quality of correction. However, this was not the case for the present study (S7
527 Fig). Importantly, as can be seen in Fig 2, high values of perfusion were tightly
528 confined to the GM ribbon illustrating the high accuracy of the segmentation and co-
529 registration in the present study.

530 **Limitations**

531 The goal of the present study was to demonstrate the feasibility of using perfusion-
532 weighted contrast with ASL for laminar fMRI and, to that end, we employed a block

533 design with a strong feed-forward visual stimulus that is known to elicit widespread
534 activation. Due to the lower SNR of the perfusion-signal, we averaged 40 min worth
535 of functional runs. While there is the undoubted benefit in spatial specificity, ASL
536 may not be well-suited for all laminar fMRI studies, particularly those with small effect
537 sizes. In addition, GE-BOLD laminar fMRI data are routinely acquired with 0.6-0.8
538 mm isotropic resolutions, higher than the current ASL study. While the use of Partial-
539 Fourier acquisition can reduce the effective spatial resolution along a dimension, the
540 amount of blurring was reduced by using POCS reconstruction algorithm instead of
541 zero-filling. Nevertheless, to the best of our knowledge, this study remains the
542 highest spatial resolution functional ASL study in humans till date. Going forward,
543 sub-millimetre resolution ASL can be invaluable to studies that are examining BOLD
544 signal physiology, for validating existing models or for brain areas contaminated by
545 close large pial veins.

546 The lowest achievable TE in the present study was 15 ms owing to the EPI readout,
547 which is not ideally suited for perfusion imaging. Although, it would be desirable to
548 achieve shorter TEs (e.g. ~3 ms or less) for better perfusion-weighting, it is currently
549 not possible using conventional Cartesian EPI. To this end, there has been recent
550 progress in non-Cartesian (e.g. spiral readouts) ASL fMRI at ultra-high field
551 [100,101]. Dual-echo spiral acquisitions can be particularly useful for simultaneous
552 perfusion and BOLD imaging achieving the first echo at ~2 ms (perfusion-weighted)
553 and the second echo at ~25 ms (BOLD) at 7T. However, these non-Cartesian
554 acquisitions are prone to inaccuracies in the spiral trajectories due to gradient
555 imperfections that require real-time monitoring and correction using specialised field-
556 monitoring hardware [100]. However, research and development are still underway

557 to address these technical challenges in non-Cartesian imaging and currently sub-
558 millimetre fMRI acquisitions have not been demonstrated.

559 We show that high-resolution ASL at ultra-high field is possible using the standard
560 commercial head-coil with single-channel transmit (NOVA Medical, USA). However,
561 the B_1^+ inhomogeneities remain a major hurdle [33]. While We were able to mitigate
562 this to some extent using dielectric pads [50,51], Future studies will be able to take
563 advantage of advances in parallel transmission (pTx) technology [102] or the use of
564 dedicated labelling-only RF-coils [103–106] to potentially further optimise high-
565 resolution ASL fMRI at ultra-high fields. Having demonstrated the feasibility of
566 perfusion-weighted laminar fMRI using ASL at a sub-millimetre spatial resolution,
567 future studies will be able to systematically evaluate different properties ASL and its
568 impact on the perfusion signal evolution at ultra-high field.

569

570 **ACKNOWLEDGEMENTS**

571 The study was supported by the Netherlands Organisation for Scientific Research
572 (NWO) VIDI grant (452-11-002) and the Institute for Basic Science, Suwon, Republic
573 of Korea (IBS-R015-D1) to K.U., NWO VENI grant (016-198-032) to L.H., NWO VIDI
574 grant (016-178-052) to and National Institutes of Health grant (R01MH111444, PI:
575 David A. Feinberg) to B.A.P. The funders had no role in study design, data collection
576 and analysis, decision to publish, or preparation of the manuscript. All data were
577 acquired at the Scannexus B.V. facilities, Maastricht, The Netherlands.

578 **REFERENCES**

- 579 1. Logothetis NK, Wandell BA. Interpreting the BOLD Signal. *Annu Rev Physiol.*
580 2004;66: 735–769. doi:10.1146/annurev.physiol.66.082602.092845
- 581 2. Uludağ K, Blinder P. Linking brain vascular physiology to hemodynamic
582 response in ultra-high field MRI. *Neuroimage.* 2018;168: 279–295.
583 doi:10.1016/j.neuroimage.2017.02.063
- 584 3. Goense J, Whittingstall K, Logothetis NK. Neural and BOLD responses across
585 the brain. *Wiley Interdiscip Rev Cogn Sci.* 2012;3: 75–86.
- 586 4. Kim S-G. Biophysics of BOLD fMRI investigated with animal models. *J Magn
587 Reson.* 2018;292: 82–89. Available:
588 <http://www.sciencedirect.com/science/article/pii/S1090780718301101>
- 589 5. Polimeni JR, Uludağ K. Neuroimaging with ultra-high field MRI: Present and
590 future. Polimeni JR, Uludag K, editors. *NeuroImage.* Elsevier; 2018.
591 doi:10.1016/j.neuroimage.2018.01.072
- 592 6. Yacoub E, Wald LL, editors. *Pushing the spatio-temporal limits of MRI and
593 fMRI.* *NeuroImage.* Elsevier; 2018.

594 doi:<https://doi.org/10.1016/j.neuroimage.2017.11.034>

595 7. Glasser MF, Coalson TS, Robinson EC, Hacker CD, Harwell J, Yacoub E, et
596 al. A multi-modal parcellation of human cerebral cortex. *Nature*. 2016;536:
597 171–178. doi:10.1038/nature18933

598 8. Brodmann K. *Vergleichende Lokalisationslehre der Grosshirnrinde in ihren
599 Prinzipien dargestellt auf Grund des Zellenbaues*. J.A. Barth; 1909.

600 9. Vogt O. *Die myeloarchitektonische Felderung des menschlichen Stirnhirns*.
601 J.A. Barth; 1910. Available:
602 <https://books.google.nl/books?id=5DFkQwAACAAJ>

603 10. Norris DG, Polimeni JR, editors. *MRI of Cortical Layers*. *NeuroImage*. Elsevier;
604 2019. doi:<https://doi.org/10.1016/j.neuroimage.2019.04.082>

605 11. Ogawa S, Lee TM, Kay AR, Tank DW. Brain magnetic resonance imaging with
606 contrast dependent on blood oxygenation. *Proc Natl Acad Sci U S A*. 1990;87:
607 9868–9872. doi:10.1073/pnas.87.24.9868

608 12. Ogawa S, Tank DW, Menon R, Ellermann JM, Kim SG, Merkle H, et al.
609 Intrinsic signal changes accompanying sensory stimulation: functional brain
610 mapping with magnetic resonance imaging. *Proc Natl Acad Sci U S A*.
611 1992;89: 5951–5955. doi:10.1073/pnas.89.13.5951

612 13. Havlicek M, Uludağ K. A dynamical model of the laminar BOLD response.
613 *Neuroimage*. 2020;204: 609099. doi:10.1016/j.neuroimage.2019.116209

614 14. Turner R. How much cortex can a vein drain? Downstream dilution of
615 activation-related cerebral blood oxygenation changes. *Neuroimage*. 2002;16:
616 1062–1067.

617 15. Lai S, Hopkins AL, Haacke EM, Li D, Wasserman BA, Buckley P, et al.
618 Identification of vascular structures as a major source of signal contrast in high

619 resolution 2D and 3D functional activation imaging of the motor cortex at 1.5T
620 preliminary results. *Magn Reson Med.* 1993;30: 387–392.
621 doi:10.1002/mrm.1910300318

622 16. Chen G, Wang F, Gore JC, Roe AW. Layer-specific BOLD activation in awake
623 monkey V1 revealed by ultra-high spatial resolution functional magnetic
624 resonance imaging. *Neuroimage.* 2013;64: 147–155.
625 doi:10.1016/j.neuroimage.2012.08.060

626 17. Harel N, Lin J, Moeller S, U\ugurbil K, Yacoub E. Combined imaging-
627 histological study of cortical laminar specificity of fMRI signals. *Neuroimage.*
628 2006;29: 879–887. doi:10.1016/j.neuroimage.2005.08.016

629 18. Jin T, Kim S-G. Cortical layer-dependent dynamic blood oxygenation, cerebral
630 blood flow and cerebral blood volume responses during visual stimulation.
631 *Neuroimage.* 2008;43: 1–9. doi:10.1016/j.neuroimage.2008.06.029

632 19. Zhao F, Wang P, Kim SG. Cortical depth-dependent gradient-echo and spin-
633 echo BOLD fMRI at 9.4T. *Magn Reson Med.* 2004;51: 518–524.
634 doi:10.1002/mrm.10720

635 20. Zhao F, Jin T, Wang P, Kim SG. Improved spatial localization of post-stimulus
636 BOLD undershoot relative to positive BOLD. *Neuroimage.* 2007;34: 1084–
637 1092. doi:10.1016/j.neuroimage.2006.10.016

638 21. Koopmans PJ, Barth M, Orzada S, Norris DG. Multi-echo fMRI of the cortical
639 laminae in humans at 7T. *Neuroimage.* 2011;56: 1276–1285.
640 doi:10.1016/j.neuroimage.2011.02.042

641 22. Marquardt I, Schneider M, Gulban OF, Ivanov D, Uludag K. Cortical depth
642 profiles of luminance contrast responses in human V1 and V2 using 7 T fMRI.
643 *Hum Brain Mapp.* 2018. doi:10.1002/hbm.24042

644 23. Heinze J, Koopmans PJ, den Ouden HEM, Raman S, Stephan KE. A
645 hemodynamic model for layered BOLD signals. *Neuroimage*. 2016;125: 556–
646 570. doi:10.1016/j.neuroimage.2015.10.025

647 24. Markuerkiaga I, Barth M, Norris DG. A cortical vascular model for examining
648 the specificity of the laminar BOLD signal. *Neuroimage*. 2016;132: 491–498.
649 doi:10.1016/j.neuroimage.2016.02.073

650 25. Donahue MJ, Lu H, Jones CK, Edden RAE, Pekar JJ, van Zijl PCM.
651 Theoretical and experimental investigation of the VASO contrast mechanism.
652 *Magn Reson Med*. 2006;56: 1261–1273.

653 26. Lu H, Golay X, Pekar JJ, Van Zijl PC. Functional magnetic resonance imaging
654 based on changes in vascular space occupancy. *Magn Reson Med*. 2003;50:
655 263–274. doi:10.1002/mrm.10519

656 27. Jin T, Kim S-G. Improved cortical-layer specificity of vascular space occupancy
657 fMRI with slab inversion relative to spin-echo BOLD at 9.4 T. *Neuroimage*.
658 2008;40: 59–67. doi:10.1016/j.neuroimage.2007.11.045

659 28. Detre JA, Leigh JS, Williams DS, Koretsky AP. Perfusion imaging. *Magn*
660 *Reson Med*. 1992;23: 37–45. doi:10.1002/mrm.1910230106

661 29. Kwong KK, Chesler DA, Weisskoff RM, Donahue KM, Davis TL, Ostergaard L,
662 et al. MR perfusion studies with T1-weighted echo planar imaging. *Magn*
663 *Reson Med*. 1995;34: 878–887. doi:10.1002/mrm.1910340613

664 30. Wong EC, Buxton RB, Frank LR. Quantitative imaging of perfusion using a
665 single subtraction (QUIPSS and QUIPSS II). *Magn Reson Med*. 1998;39: 702–
666 708.

667 31. Fukuda M, Poplawsky AJ, Kim SG. Submillimeter-resolution fMRI: Toward
668 understanding local neural processing. 2016. doi:10.1016/bs.pbr.2016.03.003

669 32. Pfeuffer J, Adriany G, Shmuel A, Yacoub E, Van De Moortele P-F, Hu X, et al.
670 Perfusion-based high-resolution functional imaging in the human brain at 7
671 Tesla. *Magn Reson Med.* 2002;47: 903–911. doi:10.1002/mrm.10154

672 33. Ivanov D, Gardumi A, Haast RAM, Pfeuffer J, Poser BA, Uludağ K.
673 Comparison of 3 T and 7 T ASL techniques for concurrent functional perfusion
674 and BOLD studies. *Neuroimage.* 2017;156: 363–376.
675 doi:10.1016/j.neuroimage.2017.05.038

676 34. Huber L, Ivanov D, Krieger SN, Streicher MN, Mildner T, Poser BA, et al. Slab-
677 selective, BOLD-corrected VASO at 7 Tesla provides measures of cerebral
678 blood volume reactivity with high signal-to-noise ratio. *Magn Reson Med.*
679 2014;72: 137–148.

680 35. Goense J, Bohraus Y, Logothetis NK. fMRI at High Spatial Resolution:
681 Implications for BOLD-Models. *Front Comput Neurosci.* 2016;10: 66.
682 doi:10.3389/fncom.2016.00066

683 36. Huber L, Handwerker DA, Jangraw DC, Chen G, Hall A, Stuber C, et al. High-
684 Resolution CBV-fMRI Allows Mapping of Laminar Activity and Connectivity of
685 Cortical Input and Output in Human M1. *Neuron.* 2017;96: 1253-1263.e7.
686 doi:10.1016/j.neuron.2017.11.005

687 37. Alsop DC, Detre JA, Golay X, Gunther M, Hendrikse J, Hernandez-Garcia L, et
688 al. Recommended implementation of arterial spin-labeled perfusion MRI for
689 clinical applications: A consensus of the ISMRM perfusion study group and the
690 European consortium for ASL in dementia. *Magn Reson Med.* 2015;73: 102–
691 116.

692 38. Gardumi A, Ivanov D, Havlicek M, Formisano E, Uludağ K. Tonotopic maps in
693 human auditory cortex using arterial spin labeling. *Hum Brain Mapp.* 2016.

694 doi:10.1002/hbm.23444

695 39. Pohmann R, Speck O, Scheffler K. Signal-to-noise ratio and MR tissue
696 parameters in human brain imaging at 3, 7, and 9.4 tesla using current receive
697 coil arrays. *Magn Reson Med.* 2016;75: 801–809. doi:10.1002/mrm.25677

698 40. Rooney WD, Johnson G, Li X, Cohen ER, Kim S-G, Ügurbil K, et al. Magnetic
699 field and tissue dependencies of human brain longitudinal $^1\text{H}_2\text{O}$ relaxation in
700 vivo. *Magn Reson Med.* 2007;57: 308–318.

701 41. Wright PJ, Mougin OE, Totman JJ, Peters AM, Brookes MJ, Coxon R, et al.
702 Water proton T1 measurements in brain tissue at 7, 3, and 1.5 T using IR-EPI,
703 IR-TSE, and MPRAGE: results and optimization. *MAGMA.* 2008;21: 121–130.

704 42. Ivanov D, Poser BA, Huber L, Pfeuffer J, Uludağ K. Optimization of
705 simultaneous multislice EPI for concurrent functional perfusion and BOLD
706 signal measurements at 7T. *Magn Reson Med.* 2016. doi:10.1002/mrm.26351

707 43. Ivanov D, Poser BA, Kashyap S, Gardumi A, Huber L, Uludağ K. Sub-
708 millimeter human brain perfusion imaging using arterial spin labelling at 3 and
709 7 Tesla. ISMRM Workshop on Ultra High Field MRI. 2016.

710 44. Zimmer F, O'Brien K, Bollmann S, Pfeuffer J, Heberlein K, Barth M. Pulsed
711 arterial spin labelling at ultra-high field with a $B_1 (+)$ -optimised adiabatic
712 labelling pulse. *MAGMA.* 2016;29: 463–473. doi:10.1007/s10334-016-0555-2

713 45. Ivanov D, Kashyap S, Haast RAM, Janssens S, Huber L, Poser BA, et al.
714 Whole-brain sub-millimeter isotropic resolution cerebral blood flow map in
715 humans. Proceedings of the 24th Annual Meeting of ISMRM. 2018.

716 46. Kashyap S, Ivanov D, Havlicek M, Poser BA, Uludağ K, Uludag K. Laminar
717 CBF and BOLD fMRI in the human visual cortex using arterial spin labelling at
718 7T. Proc 27th Sci Meet ISMRM. 2019; 609.

719 47. Hurley AC, Al-Radaideh A, Bai L, Aickelin U, Coxon R, Glover P, et al. Tailored
720 RF Pulse for Magnetization Inversion at Ultrahigh Field. *Magn Reson Med.*
721 2010;63: 51–58.

722 48. Webb AG. Dielectric materials in magnetic resonance. *Concepts Magn Reson*
723 Part A. 2011;38A: 148–184. doi:doi:10.1002/cmr.a.20219

724 49. Poser BA, Koopmans PJ, Witzel T, Wald LL, Barth M. Three dimensional
725 echo-planar imaging at 7 Tesla. *Neuroimage.* 2010;51: 261–266.
726 doi:10.1016/j.neuroimage.2010.01.108

727 50. Haines K, Smith NB, Webb AG. New high dielectric constant materials for
728 tailoring the B1+ distribution at high magnetic fields. *J Magn Reson.* 2010;203:
729 323–327. Available:
730 <http://www.sciencedirect.com/science/article/pii/S1090780710000042>

731 51. Teeuwisse WM, Brink WM, Webb AG. Quantitative assessment of the effects
732 of high-permittivity pads in 7 Tesla MRI of the brain. *Magn Reson Med.*
733 2012;67: 1285–1293.

734 52. Peirce JW. PsychoPy--Psychophysics software in Python. *J Neurosci*
735 Methods. 2007;162: 8–13. doi:10.1016/j.jneumeth.2006.11.017

736 53. Marques JP, Kober T, Krueger G, van der Zwaag W, Van de Moortele PF,
737 Gruetter R. MP2RAGE, a self bias-field corrected sequence for improved
738 segmentation and T1-mapping at high field. *Neuroimage.* 2010;49: 1271–
739 1281. doi:10.1016/j.neuroimage.2009.10.002

740 54. Kim S-G. Quantification of relative cerebral blood flow change by flow-sensitive
741 alternating inversion recovery (FAIR) technique: Application to functional
742 mapping. *Magn Reson Med.* 1995;34: 293–301. doi:10.1002/mrm.1910340303

743 55. Talagala SL, Sarlls JE, Liu S, Inati SJ. Improvement of temporal signal-to-

744 noise ratio of GRAPPA accelerated echo planar imaging using a FLASH based
745 calibration scan. *Magn Reson Med.* 2016;75: 2362–2371.
746 doi:10.1002/mrm.25846

747 56. Haacke EM, Lindskog ED, Lin W. A Fast, Iterative, Partial-Fourier Technique
748 Capable of Local Phase Recovery. *J Magn Reson.* 1991;92: 126–145. doi:Doi
749 10.1016/0022-2364(91)90253-P

750 57. Penny WD, Friston KJ, Ashburner JT, Kiebel SJ, Nichols TE. *Statistical*
751 *Parametric Mapping: The Analysis of Functional Brain Images.* Elsevier
752 Science; 2011. Available: https://books.google.nl/books?id=G_qdEsDlkp0C

753 58. Ashburner J. SPM: a history. *Neuroimage.* 2012;62: 791–800.
754 doi:10.1016/j.neuroimage.2011.10.025

755 59. Smith SM, Jenkinson M, Woolrich MW, Beckmann CF, Behrens TE,
756 Johansen-Berg H, et al. Advances in functional and structural MR image
757 analysis and implementation as FSL. *Neuroimage.* 2004;23 Suppl 1: S208-19.
758 doi:10.1016/j.neuroimage.2004.07.051

759 60. Jenkinson M, Beckmann CF, Behrens TEJ, Woolrich MW, Smith SM. FSL.
760 *Neuroimage.* 2012;62: 782–790. doi:10.1016/j.neuroimage.2011.09.015

761 61. Ashburner J, Friston KJ. Unified segmentation. *Neuroimage.* 2005;26: 839–
762 851. doi:10.1016/j.neuroimage.2005.02.018

763 62. Smith SM. Fast robust automated brain extraction. *Hum Brain Mapp.* 2002;17:
764 143–155.

765 63. Fischl B. FreeSurfer. *Neuroimage.* 2012;62: 774–781.
766 doi:10.1016/j.neuroimage.2012.01.021

767 64. Benson NC, Winawer J. Bayesian analysis of retinotopic maps. Schira M, Gold
768 JI, editors. *Elife.* 2018;7: e40224. doi:10.7554/eLife.40224

769 65. Fujimoto K, Polimeni JR, van der Kouwe AJW, Reuter M, Kober T, Benner T,
770 et al. Quantitative comparison of cortical surface reconstructions from
771 MP2RAGE and multi-echo MPRAGE data at 3 and 7T. *Neuroimage*. 2014;90:
772 60–73. doi:<https://doi.org/10.1016/j.neuroimage.2013.12.012>

773 66. Wagstyl K, Lepage C, Bludau S, Zilles K, Fletcher PC, Amunts K, et al.
774 Mapping Cortical Laminar Structure in the 3D BigBrain. *Cereb Cortex*.
775 2018;28: 2551–2562. doi:[10.1093/cercor/bhy074](https://doi.org/10.1093/cercor/bhy074)

776 67. Avants BB, Tustison NJ, Wu J, Cook PA, Gee JC. An open source multivariate
777 framework for n-tissue segmentation with evaluation on public data.
778 *Neuroinformatics*. 2011;9: 381–400. doi:[10.1007/s12021-011-9109-y](https://doi.org/10.1007/s12021-011-9109-y)

779 68. Avants BB, Tustison NJ, Song G, Cook PA, Klein A, Gee JC. A reproducible
780 evaluation of ANTs similarity metric performance in brain image registration.
781 *Neuroimage*. 2011;54: 2033–2044. doi:[10.1016/j.neuroimage.2010.09.025](https://doi.org/10.1016/j.neuroimage.2010.09.025)

782 69. Yushkevich PA, Piven J, Hazlett HC, Smith RG, Ho S, Gee JC, et al. User-
783 guided 3D active contour segmentation of anatomical structures: significantly
784 improved efficiency and reliability. *Neuroimage*. 2006;31: 1116–1128.
785 doi:[10.1016/j.neuroimage.2006.01.015](https://doi.org/10.1016/j.neuroimage.2006.01.015)

786 70. Polimeni JR, Renvall V, Zaretskaya N, Fischl B. Analysis strategies for high-
787 resolution UHF-fMRI data. *Neuroimage*. 2018;168: 296–320.
788 doi:[10.1016/j.neuroimage.2017.04.053](https://doi.org/10.1016/j.neuroimage.2017.04.053)

789 71. Woolrich MW, Behrens TE, Beckmann CF, Jenkinson M, Smith SM. Multilevel
790 linear modelling for fMRI group analysis using Bayesian inference.
791 *Neuroimage*. 2004;21: 1732–1747. doi:[10.1016/j.neuroimage.2003.12.023](https://doi.org/10.1016/j.neuroimage.2003.12.023)

792 72. Worsley KJ. Statistical analysis of activation images. *Funct MRI An Introd to*
793 *methods*. 2001;14: 251–270.

794 doi:10.1093/acprof:oso/9780192630711.003.0014

795 73. Havlicek M, Roebroeck A, Friston KJ, Gardumi A, Ivanov D, Uludag K. On the
796 importance of modeling fMRI transients when estimating effective connectivity:
797 A dynamic causal modeling study using ASL data. *Neuroimage*. 2017;155:
798 217–233. doi:<https://doi.org/10.1016/j.neuroimage.2017.03.017>

799 74. Aguirre GK, Detre JA, Zarahn E, Alsop DC. Experimental design and the
800 relative sensitivity of BOLD and perfusion fMRI. *Neuroimage*. 2002;15: 488–
801 500. doi:[10.1006/nimg.2001.0990](https://doi.org/10.1006/nimg.2001.0990)

802 75. Liu TT, Wong EC. A signal processing model for arterial spin labeling
803 functional MRI. *Neuroimage*. 2005;24: 207–215.
804 doi:<https://doi.org/10.1016/j.neuroimage.2004.09.047>

805 76. Cavusoglu M, Pfeuffer J, Uğurbil K, Uludağ K. Comparison of pulsed arterial
806 spin labeling encoding schemes and absolute perfusion quantification. *Magn
807 Reson Imaging*. 2009;27: 1039–1045. doi:[10.1016/j.mri.2009.04.002](https://doi.org/10.1016/j.mri.2009.04.002)

808 77. Buxton RB, Uludağ K, Dubowitz DJ, Liu TT. Modeling the hemodynamic
809 response to brain activation. *Neuroimage*. 2004;23: S220-33.
810 doi:[10.1016/j.neuroimage.2004.07.013](https://doi.org/10.1016/j.neuroimage.2004.07.013)

811 78. Chai Y, Li L, Huber L, Poser BA, Bandettini PA. Integrated VASO and
812 perfusion contrast: A new tool for laminar functional MRI. *Neuroimage*.
813 2020;207: 116358. doi:<https://doi.org/10.1016/j.neuroimage.2019.116358>

814 79. Huber L, Uludağ K, Moller HE. Non-BOLD contrast for laminar fMRI in
815 humans: CBF, CBV, and CMRO₂. *Neuroimage*. 2017.
816 doi:[10.1016/j.neuroimage.2017.07.041](https://doi.org/10.1016/j.neuroimage.2017.07.041)

817 80. Guidi M, Huber L, Lampe L, Gauthier CJ, Moller HE. Lamina-dependent
818 calibrated BOLD response in human primary motor cortex. *Neuroimage*.

819 2016;141: 250–261. doi:10.1016/j.neuroimage.2016.06.030

820 81. Lu H, Hua J, van Zijl PCM. Noninvasive functional imaging of cerebral blood
821 volume with vascular-space-occupancy (VASO) MRI. *NMR Biomed.* 2013;26:
822 932–948. doi:10.1002/nbm.2905

823 82. Wong EC, Buxton RB, Frank LR. Implementation of quantitative perfusion
824 imaging techniques for functional brain mapping using pulsed arterial spin
825 labeling. *NMR Biomed.* 1997;10: 237–249.

826 83. Wang J, Alsop DC, Song HK, Maldjian JA, Tang K, Salvucci AE, et al. Arterial
827 transit time imaging with flow encoding arterial spin tagging (FEAST). *Magn
828 Reson Med.* 2003;50: 599–607.

829 84. Kashyap S, Ivanov D, Havlicek M, Poser BA, Uludağ K. Impact of acquisition
830 and analysis strategies on cortical depth-dependent fMRI. *Neuroimage.*
831 2018;168: 332–344. doi:10.1016/j.neuroimage.2017.05.022

832 85. Polimeni JR, Fischl B, Greve DN, Wald LL. Laminar analysis of 7T BOLD
833 using an imposed spatial activation pattern in human V1. *Neuroimage.*
834 2010;52: 1334–1346. doi:10.1016/j.neuroimage.2010.05.005

835 86. De Martino F, Zimmermann J, Muckli L, U\ugurbil K, Yacoub E, Goebel R.
836 Cortical Depth Dependent Functional Responses in Humans at 7T: Improved
837 Specificity with 3D GRASE. *PLoS One.* 2013;8: 30–32.
838 doi:10.1371/journal.pone.0060514

839 87. Fracasso A, Luijten PR, Dumoulin SO, Petridou N. Laminar imaging of positive
840 and negative BOLD in human visual cortex at 7T. *Neuroimage.* 2018.
841 doi:10.1016/j.neuroimage.2017.02.038

842 88. Kashyap S, Ivanov D, Havlicek M, Sengupta S, Poser BA, Uludağ K.
843 Resolving laminar activation in human V1 using ultra-high spatial resolution

844 fMRI at 7T. *Sci Rep.* 2018;8. doi:10.1038/s41598-018-35333-3

845 89. Yen CC, Papoti D, Silva AC. Investigating the spatiotemporal characteristics of
846 the deoxyhemoglobin-related and deoxyhemoglobin-unrelated functional
847 hemodynamic response across cortical layers in awake marmosets.
848 *Neuroimage.* 2018;164: 121–130. doi:10.1016/j.neuroimage.2017.03.005

849 90. Tootell RB, Hamilton SL, Switkes E. Functional anatomy of macaque striate
850 cortex. IV. Contrast and magno-parvo streams. *J Neurosci.* 1988;8: 1594–
851 1609. doi:10.1523/JNEUROSCI.08-05-01594.1988

852 91. Duong TQ, Kim DS, Uğurbil K, Kim SG. Spatiotemporal dynamics of the BOLD
853 fMRI signals: Toward mapping submillimeter cortical columns using the early
854 negative response. *Magn Reson Med.* 2000;44: 231–242.

855 92. Silva AC, Lee SP, Iadecola C, Kim SG. Early temporal characteristics of
856 cerebral blood flow and deoxyhemoglobin changes during somatosensory
857 stimulation. *J Cereb blood flow Metab Off J Int Soc Cereb Blood Flow Metab.*
858 2000;20: 201–206. doi:10.1097/00004647-200001000-00025

859 93. Siero JC, Hendrikse J, Hoogduin H, Petridou N, Luijten P, Donahue MJ.
860 Cortical depth dependence of the BOLD initial dip and poststimulus
861 undershoot in human visual cortex at 7 Tesla. *Magn Reson Med.* 2015;73:
862 2283–2295.

863 94. Mullinger KJ, Mayhew SD, Bagshaw AP, Bowtell R, Francis ST. Poststimulus
864 undershoots in cerebral blood flow and BOLD fMRI responses are modulated
865 by poststimulus neuronal activity. *Proc Natl Acad Sci U S A.* 2013;110: 13636–
866 13641. doi:10.1073/pnas.1221287110

867 95. Berwick J, Johnston D, Jones M, Martindale J, Martin C, Kennerley AJ, et al.
868 Fine Detail of Neurovascular Coupling Revealed by Spatiotemporal Analysis of

869 the Hemodynamic Response to Single Whisker Stimulation in Rat Barrel
870 Cortex. J Neurophysiol. 2008;99: 787–798. doi:10.1152/jn.00658.2007

871 96. Waehnert MD, Dinse J, Weiss M, Streicher MN, Waehnert P, Geyer S, et al.
872 Anatomically motivated modeling of cortical laminae. Neuroimage. 2014;93 Pt
873 2: 210–220. doi:10.1016/j.neuroimage.2013.03.078

874 97. Wagstyl K, Paquola C, Bethlehem R, Evans AC, Huth A. Equivolumetric
875 layering for mesh surfaces. 2018. doi:10.5281/zenodo.1442584

876 98. Kemper VG, De Martino F, Emmerling TC, Yacoub E, Goebel R. High
877 resolution data analysis strategies for mesoscale human functional MRI at 7
878 and 9.4T. Neuroimage. 2018;164: 48–58.
879 doi:10.1016/j.neuroimage.2017.03.058

880 99. Glasser MF, Sotiropoulos SN, Wilson JA, Coalson TS, Fischl B, Andersson JL,
881 et al. The minimal preprocessing pipelines for the Human Connectome Project.
882 Neuroimage. 2013;80: 105–124. doi:10.1016/j.neuroimage.2013.04.127

883 100. Engel M, Kasper L, Barmet C, Schmid T, Vionnet L, Wilm B, et al. Single-shot
884 spiral imaging at 7 T. Magn Reson Med. 2018;80: 1836–1846.

885 101. Kurban D, Liberman G, Kashyap S, Ivanov D, Poser BA. Simultaneous multi-
886 slice spiral acquisitions for CBF fMRI at 7T. Proceedings of the ISMRM
887 Workshop on Ultrahigh Field Magnetic Resonance. 2019.

888 102. Adriany G, de Moortele PF, Wiesinger F, Moeller S, Strupp JP, Andersen P, et
889 al. Transmit and receive transmission line arrays for 7 Tesla parallel imaging.
890 Magn Reson Med. 2005;53: 434–445. doi:10.1002/mrm.20321

891 103. Alsaedi A, Thomas D, Bisdas S, Golay X. Overview and Critical Appraisal of
892 Arterial Spin Labelling Technique in Brain Perfusion Imaging. Contrast Media
893 Mol Imaging. 2018;2018: 15. doi:10.1155/2018/5360375

894 104. Aslan S, Xu F, Wang PL, Uh J, Yezhuvath US, van Osch M, et al. Estimation
895 of labeling efficiency in pseudocontinuous arterial spin labeling. *Magn Reson*
896 *Med.* 2010;63: 765–771.

897 105. Luh WM, Talagala SL, Li TQ, Bandettini PA. Pseudo-continuous arterial spin
898 labeling at 7 T for human brain\$\backslash\$backslashcolon{\$\backslash\$} estimation and correction
899 for off-resonance effects using a Prescan. *Magn Reson Med.* 2012/04/09.
900 2013;69: 402–410. Available:
901 <https://www.ncbi.nlm.nih.gov/pmc/articles/PMC3402610/>

902 106. Mora Alvarez MG, Stobbe RW, Beaulieu C. High resolution continuous arterial
903 spin labeling of human cerebral perfusion using a separate neck tagging RF
904 coil. *PLoS One.* 2019;14. doi:10.1371/journal.pone.0215998

905 **DATA AND CODE AVAILABILITY STATEMENT**

906 The authors do not have permission to share the data. The 3D-EPI PASL sequence
907 used to acquire the data is available upon request via a SIEMENS C2P agreement.
908 All code used for analysis are either already publicly available or will be made
909 available upon publication.

910 **FIGURES**

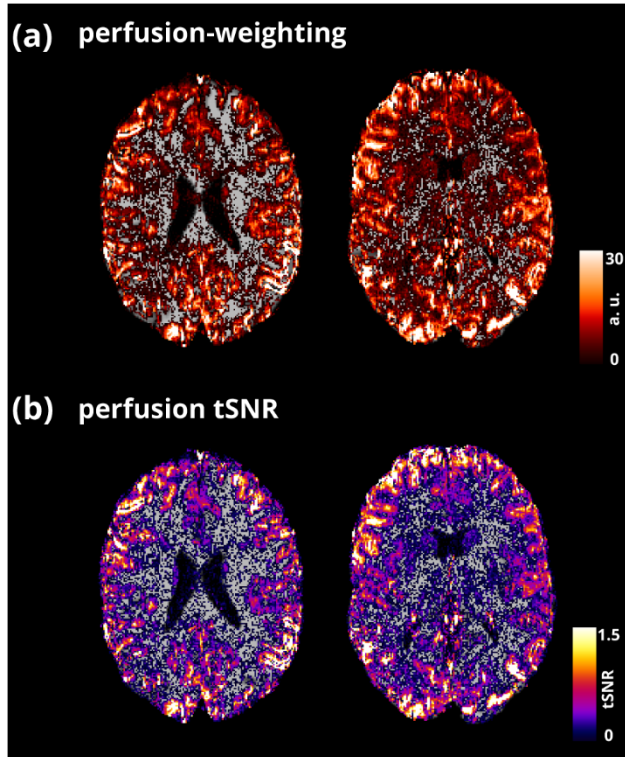
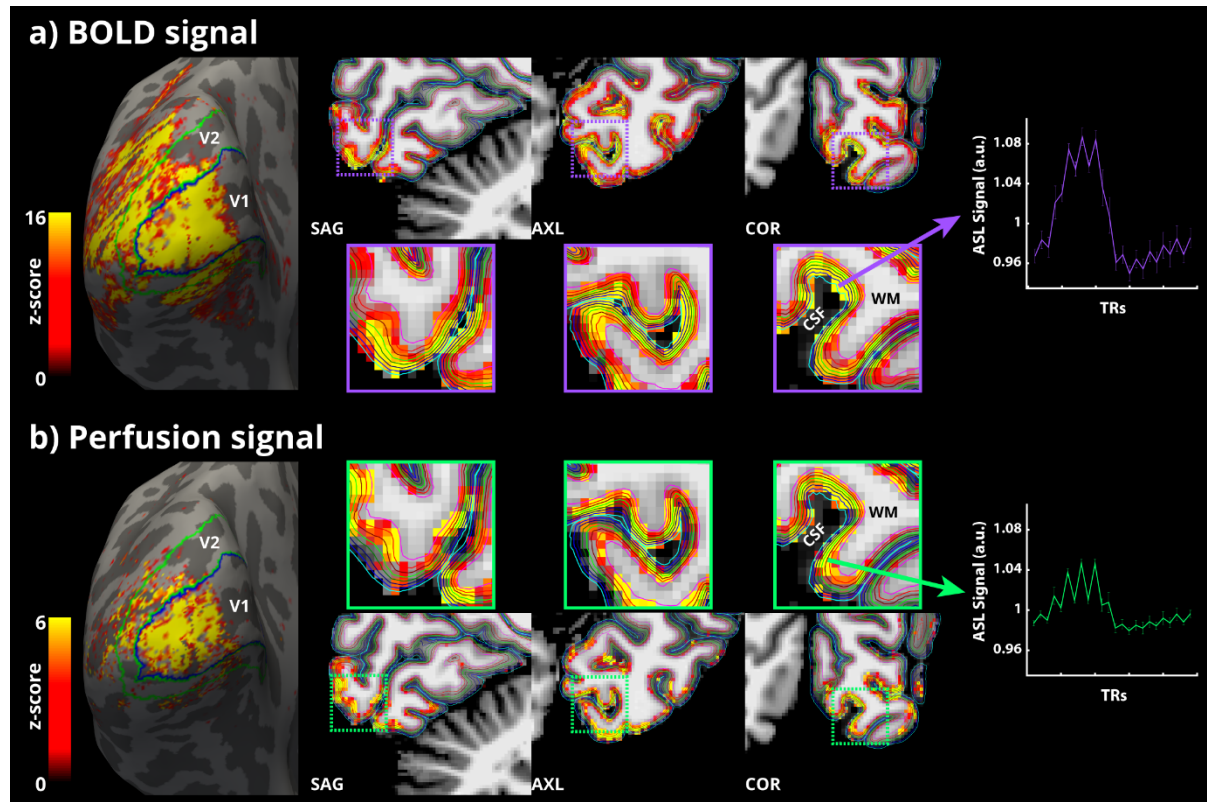
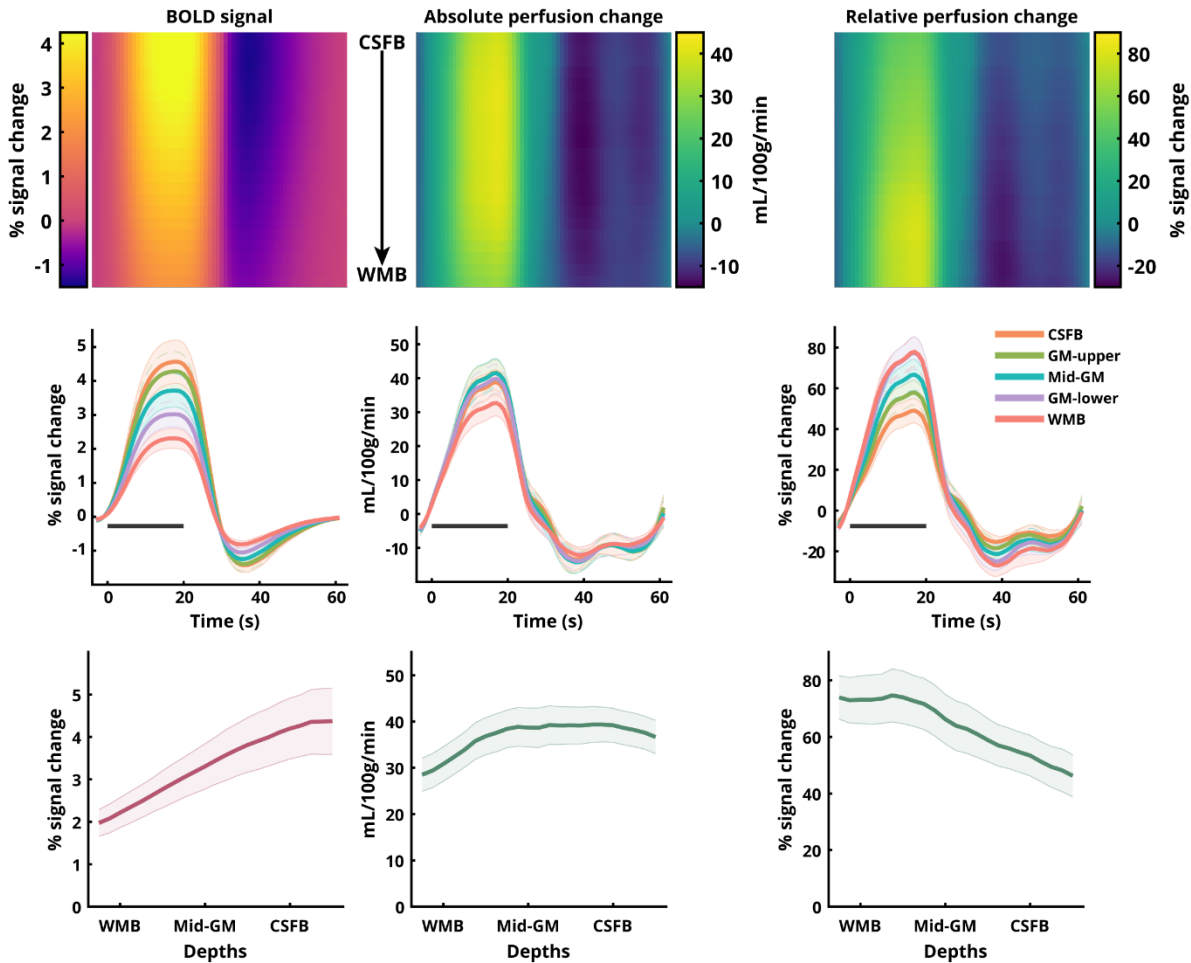


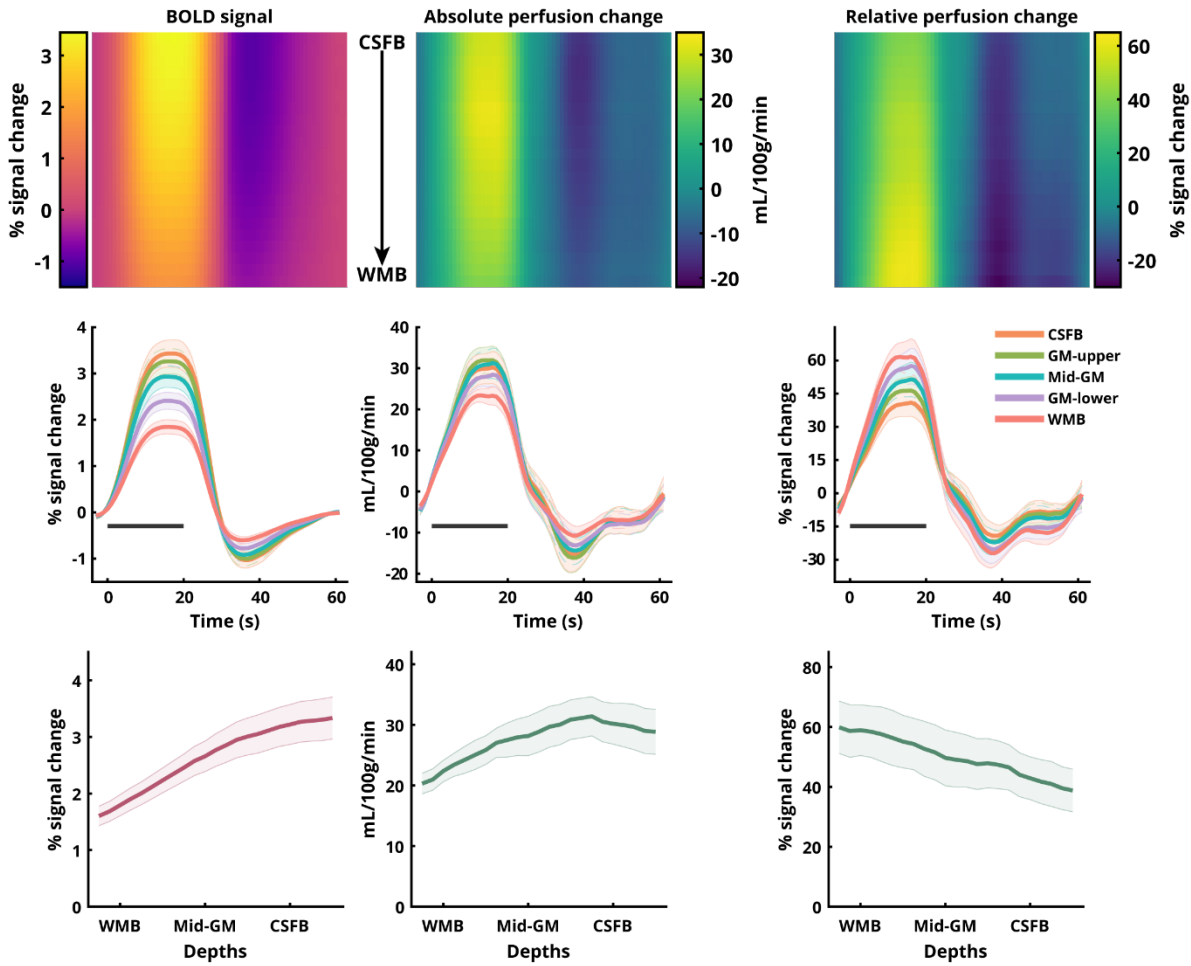
Fig 1. The average baseline perfusion (a) and perfusion tSNR (b) maps from a superior (left) and inferior (right) slice of an example participant is shown overlaid on the corresponding T₁-w anatomy.





929

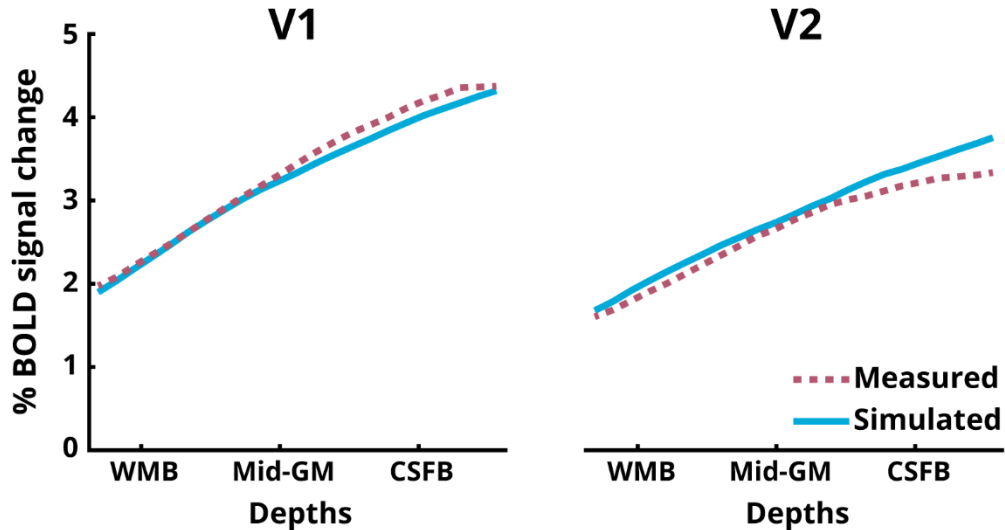
930 Fig 3. Laminar BOLD and perfusion signal changes in human V1 ROI obtained using
931 sub-millimetre 3D-EPI ASL at 7T. (top row) Heatmap representations of the group-
932 average BOLD signal change, absolute perfusion change, and relative perfusion
933 change with cortical depth along Y-axis and time along the X-axis. (middle row) Five
934 out of the twenty-three total laminar time-courses for the respective sampled signals.
935 (bottom row) Laminar profiles of the positive responses for the respective sampled
936 signals with cortical depth along X-axis. Error-bars indicate SEM across participants.
937 The black bar in the middle row indicates the stimulus duration.



939 Fig 4. same as Fig 3 for V2 ROI.

940

941



942

943 Fig 5. Laminar profiles of the BOLD signal for V1 and V2 ROIs. The measured
944 responses are the same as the BOLD signal profiles in Fig 3 and 4. The simulated
945 profiles are obtained using the dynamical laminar BOLD model [13].